



HAL
open science

Weak Lensing of Type Ia Supernovae from the Dark Energy Survey

E. Macaulay, D. Bacon, R.C. Nichol, T.M. Davis, J. Elvin-Poole, D. Brout, D. Carollo, K. Glazebrook, S.R. Hinton, G.F. Lewis, et al.

► **To cite this version:**

E. Macaulay, D. Bacon, R.C. Nichol, T.M. Davis, J. Elvin-Poole, et al.. Weak Lensing of Type Ia Supernovae from the Dark Energy Survey. *Mon.Not.Roy.Astron.Soc.*, 2020, 496 (3), pp.4051-4059. 10.1093/mnras/staa1852 . hal-02911936

HAL Id: hal-02911936

<https://hal.science/hal-02911936>

Submitted on 24 May 2024

HAL is a multi-disciplinary open access archive for the deposit and dissemination of scientific research documents, whether they are published or not. The documents may come from teaching and research institutions in France or abroad, or from public or private research centers.

L'archive ouverte pluridisciplinaire **HAL**, est destinée au dépôt et à la diffusion de documents scientifiques de niveau recherche, publiés ou non, émanant des établissements d'enseignement et de recherche français ou étrangers, des laboratoires publics ou privés.

Weak lensing of Type Ia Supernovae from the Dark Energy Survey

E. Macaulay^{1,2*}, D. Bacon,² R. C. Nichol,² T. M. Davis³, J. Elvin-Poole,^{4,5}
 D. Brout,^{6,7} D. Carollo,^{6,8} K. Glazebrook,⁹ S. R. Hinton,³ G. F. Lewis,¹⁰ C. Lidman,¹¹
 A. Möller,¹² M. Sako,⁷ D. Scolnic,¹³ M. Smith,¹⁴ N. E. Sommer,¹¹ B. E. Tucker,¹¹
 T. M. C. Abbott,¹⁵ M. Aguena,^{16,17} J. Annis,¹⁸ S. Avila,¹⁹ E. Bertin,^{20,21} S. Bhargava,²²
 D. Brooks,²³ D. L. Burke,^{24,25} A. Carnero Rosell,²⁶ M. Carrasco Kind,^{27,28}
 J. Carretero,²⁹ F. J. Castander,^{30,31} M. Costanzi,^{32,33} L. N. da Costa,^{17,34} S. Desai,³⁵
 H. T. Diehl,¹⁸ P. Doel,²³ B. Flaugher,¹⁸ R. J. Foley,³⁶ J. García-Bellido,¹⁹
 E. Gaztanaga,^{30,31} D. W. Gerdes,^{37,38} D. Gruen,^{24,25,39} R. A. Gruendl,^{27,28}
 J. Gschwend,^{17,34} G. Gutierrez,¹⁸ D. L. Hollowood,³⁶ K. Honscheid,^{4,5} D. Huterer,³⁸
 D. J. James,⁴⁰ K. Kuehn,^{41,42} N. Kuropatkin,¹⁸ O. Lahav,²³ M. Lima,^{16,17}
 M. A. G. Maia,^{17,34} J. L. Marshall,⁴³ P. Melchior,⁴⁴ F. Menanteau,^{27,28} R. Miquel,^{45,29}
 A. Palmese,^{18,46} A. A. Plazas,⁴⁴ A. K. Romer,²² A. Roodman,^{24,25} E. Sanchez,²⁶
 V. Scarpine,¹⁸ M. Schubnell,³⁸ S. Serrano,^{30,31} I. Sevilla-Noarbe,²⁶ M. Soares-Santos,⁴⁷
 E. Suchyta,⁴⁸ M. E. C. Swanson,²⁸ G. Tarle,³⁸ T. N. Varga,^{49,50} A. R. Walker,¹⁵
 and J. Weller^{49,50} (DES Collaboration)

Affiliations are listed at the end of the paper

Accepted 2020 June 19. Received 2020 June 16; in original form 2020 March 25

ABSTRACT

We consider the effects of weak gravitational lensing on observations of 196 spectroscopically confirmed Type Ia Supernovae (SNe Ia) from years 1 to 3 of the Dark Energy Survey (DES). We simultaneously measure both the angular correlation function and the non-Gaussian skewness caused by weak lensing. This approach has the advantage of being insensitive to the intrinsic dispersion of SNe Ia magnitudes. We model the amplitude of both effects as a function of σ_8 , and find $\sigma_8 = 1.2^{+0.9}_{-0.8}$. We also apply our method to a subsample of 488 SNe from the Joint Light-curve Analysis (JLA; chosen to match the redshift range we use for this work), and find $\sigma_8 = 0.8^{+1.1}_{-0.7}$. The comparable uncertainty in σ_8 between DES–SN and the larger number of SNe from JLA highlights the benefits of homogeneity of the DES–SN sample, and improvements in the calibration and data analysis.

Key words: cosmological parameters – cosmology: observations – large-scale structure of the universe.

1 INTRODUCTION

Weak gravitational lensing (WL) is a key technique in observational cosmology (e.g. Wittman et al. 2000; Schrabback et al. 2010; Heymans et al. 2012; Hildebrandt et al. 2017), and also a key target of the Dark Energy Survey (DES; The Dark Energy Survey Collaboration 2005; Abbott et al. 2016; Becker et al. 2016; Abbott et al. 2018; Omori et al. 2018; Baxter et al. 2019). Since WL

is sensitive to space-like perturbations to the background cosmological metric, WL observations are a crucial cosmological test of theories of modified gravity (e.g. Schimd, Uzan & Riazuelo 2005; Schimd et al. 2007; Schmidt 2008; Tsujikawa & Tatekawa 2008).

The most established method of WL is the measurement of coherent distortions in the shapes of galaxies, particularly the shear (e.g. Joudaki et al. 2017; Troxel et al. 2018; Zuntz et al. 2018). WL has also been detected in observations of the Cosmic Microwave Background (CMB; e.g. Omori et al. 2018; Planck Collaboration VIII 2018b).

* E-mail: edward.macaulay@gmail.com

WL is also expected to affect the magnitudes of standard candles. Magnification due to WL has been detected in quasars (e.g. Scranton et al. 2005; Bauer et al. 2011), and also studied with Type Ia Supernovae (SNe Ia; e.g. Wambsganss et al. 1997; Valageas 2000; Wang & Mukherjee 2004; Wang 2005; Dodelson & Vallinotto 2006). We note that WL is also expected to affect gravitational-wave standard sirens, e.g. Shang & Haiman (2011) and Liao et al. (2017).

Overdense lines of sight enhance the focus of light rays, causing a magnification in the observed brightness, whereas underdense lines of sight lead to a de-magnification. Smith et al. (2014) estimated the expected lensing magnification of SNe in the Joint Light-curve Analysis (JLA) SN sample (Betoule et al. 2014). The expected lensing magnification for each SN was calculated by integrating the line-of-sight densities of galaxies observed by the Sloan Digital Sky Survey (SDSS) Baryon Oscillation Spectroscopic Survey (Dawson et al. 2013). A correlation between the magnitude residuals and the expected lensing signal was found at the 1.7σ confidence level.

Since most lines of sight in the universe are underdense, and only rare lines of sight are overdense, WL causes a characteristic skewness in the distribution of magnitude residuals of standard candles. The amount of lensing skewness depends on the contrast between voids and overdensities, and as such depends on Ω_m and σ_8 .

To provide fast calculations of 1D lensing statistics, Kainulainen & Marra (2009) developed the `turboGL` code, which was developed further in Kainulainen & Marra (2011). These lensing statistics were the basis for a series of papers developing a method to estimate the likelihood of the lensing distribution of a SN sample (MeMo, ‘the Method of the Moments’; Marra, Quartin & Amendola 2013; Quartin, Marra & Amendola 2014).

Instead of enforcing a fiducial distribution for the SN magnitude residuals, MeMo is based on empirical fitting functions for the first, second, third, and fourth moments of the residuals of SNe distance measurements, which have been calibrated to N-body simulations as a function of redshift and parameters Ω_m , σ_8 , and the intrinsic dispersion in SN magnitudes, σ_{int} . In Castro & Quartin (2014), MeMo was applied to the JLA sample, finding $\sigma_8 = 0.84^{+0.28}_{-0.65}$ (at the one-standard deviation confidence level).

The effect of WL on SN magnitudes shares some similarities with the effects of Peculiar Velocities (PVs), although there are also some significant contrasts (Gordon, Land & Slosar 2007; Neill, Hudson & Conley 2007; Davis et al. 2011; Castro, Quartin & Benitez-Herrera 2016; Garcia, Quartin & Siffert 2019). Both effects are sensitive to cosmological density fluctuations. However, PVs are sensitive to large-scale (\sim Gpc) density fluctuations, whereas WL is most sensitive to far smaller ($<$ Mpc) scales.

Although WL directly affects the observed magnitudes, PVs mainly¹ affect the redshift; the apparent effect on the magnitude residual is due to comparing the theoretical magnitude at the PV-affected redshift, instead of the ‘true’ cosmological redshift.

While both effects are similar in magnitude at $z \sim 0.2$, PVs dominate at lower redshifts, while WL becomes dominant at higher redshifts. Over the redshift range $0.1 < z < 0.3$, the two effects are similar in magnitude (Macaulay et al. 2017).

Since many SNe in the JLA catalogue are within this redshift range, in Macaulay et al. (2017) we built on the WL MeMo method to include the effects of PVs on the moments of magnitude residuals. Modelling both PVs and WL allows for a simultaneous test of the

¹There is a direct effect on the observed magnitude from the ‘ $(1+z)$ ’ term in the luminosity distance, although this is not the dominant effect.

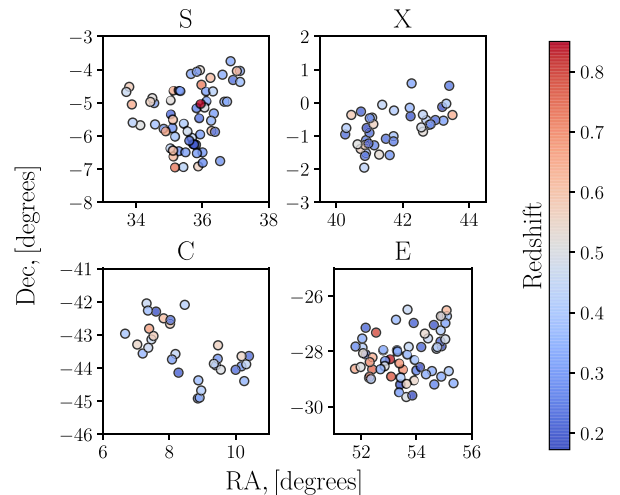


Figure 1. The angular coordinates of the four DES supernova fields. Due to the large angular separations between fields, we do not consider correlations between different fields. The points have been colour-coded by redshift; blue for lowest z , and red for highest z .

consistency of Newtonian and lensing metric perturbations, which is a key prediction of the Λ CDM model (e.g. Hu & Jain 2004; Knox, Song & Tyson 2006; Kunz & Sapone 2007; Zhang et al. 2007; Bertschinger & Zukin 2008; Simpson et al. 2013).

However, in this paper, we consider only the effects of WL, since the effect of PVs is sub-dominant, due to the absence of low redshift ($z < 0.2$) SNe in the DES–SN sample.

In addition to the effect on the moments of residuals, WL also causes correlations in the magnitudes. Scovacricchi et al. (2017) modelled the signal-to-noise ratio of the lensing correlation function, and forecast the signal-to-noise ratio of a WL detection by LSST. Scovacricchi et al. (2017) showed that for a SN survey the size of DES–SN (196 SN), the effects of WL on the correlation function would not be detectable. Nevertheless, measurements of the correlation function (however noisy), may still place upper limits on the effect of WL on the magnitude residuals.

Since the correlation function is (in principle) independent of the skewness, we can combine both observations. However, we may expect covariance between the two different types of measurements, since both observations are drawn from the same sample of data. To account for any covariance, we build on the bootstrap resampling method used in Macaulay et al. (2017) to allow for two different types of observable. We describe this method further, as well as the relevant theory and details of the observations, in Section 2. We discuss our results and conclusions in Section 3.

2 DATA AND METHODOLOGY

We study 196 new spectroscopically confirmed SNe Ia from the DES. The observation and reduction of the sample is described in a series of papers in Brout et al. (2019a,b), D’Andrea et al. (2018), Lasker et al. (2019), and Kessler et al. (2019). The cosmological analysis of the sample is described in Abbott et al. (2019), who found a value of $\Omega_m = 0.331 \pm 0.038$ for a flat Λ CDM cosmology. This is the fiducial cosmology we assume throughout this work.

We illustrate the angular coordinates of the SNe in Fig. 1.

The SNe are located in the four DES SNe fields, chosen to overlap with other well-studied fields: ‘S’ (SDSS Stripe 82), ‘X’ (XMM-LSS), ‘C’ (Chandra Deep Field South), ‘E’ (Elais-S1).

We also compare our results from DES–SN to SN from the JLA sample (Betoule et al. 2014). The full JLA sample consists of 740 SNe spanning a redshift range up to $z = 1.4$. We consider only a sub-sample of 488 in the redshift range of our lensing model, $0.2 < z < 0.5$.

For both DES–SN and JLA, we consider the distance–redshift relation fixed (using the best-fit cosmology for each survey), since the ~ 10 per cent uncertainty in the distance–redshift relation is small compared to the ~ 100 per cent uncertainty in the lensing signal.

We consider two different effects caused by WL on SN magnitudes: the correlation in the residuals (due to the fact that the lensing signal will be similar for close lines of sight), and the skewness (caused by the asymmetry of over and underdensities of dark matter). We anticipate that with the final SN sample from DES, the correlation function will be of particular interest, due to the high angular density of the SN in the small area (30 deg^2) of the SN survey. We base our treatment of the skewness on the MeMo approach (Marra, Quartin & Amendola 2013; Castro & Quartin 2014; Quartin, Marra & Amendola 2014).

2.1 MeMo

MeMo is based on minimizing the χ^2 given by

$$\chi^2 = \sum_i \Delta \boldsymbol{\mu}_i \mathbf{C}_i^{-1} \Delta \boldsymbol{\mu}_i^T, \quad (1)$$

where $\Delta \boldsymbol{\mu}_i$ is a vector given by

$$\Delta \boldsymbol{\mu}_i = \boldsymbol{\mu}_i^{\text{Obs}} - \boldsymbol{\mu}_i^{\text{MeMo}}. \quad (2)$$

Here, $\boldsymbol{\mu}_i^{\text{Obs}}$ is a vector of the observed first, second, third, and fourth moments of the distance moduli of the SN within the i th redshift bin, and \mathbf{C}_i is the corresponding data covariance matrix of this vector. $\boldsymbol{\mu}_i^{\text{MeMo}}$ is the theoretical expectation from the MeMo fitting functions.

The theoretical expectations for the moments are calculated from fitting functions, in terms of z , Ω_m , and σ_8 . The fitting functions for the second, third, and fourth moments are shown in full in equations (6), (7), and (8) in Marra et al. (2013). We note that the even moments both depend on the intrinsic dispersion of SN magnitudes, whereas – under the assumption that the intrinsic dispersion is Gaussian – the third moment depends only on the cosmological parameters.

The functions are based on the `turboGL` code, and tested against simulation results by Hilbert et al. (2008) and Takahashi et al. (2011). This approach has the advantage of computational efficiency in evaluating the moments, however, it is limited to the range of parameters used to evaluate the moments, and the cosmological model used in the simulations (flat Λ CDM).

Castro et al. (2018) used simulations to study the effect of baryonic physics on 1-point lensing statistics, finding that the effect of baryons could double the probability of highly lensed objects.

In Castro & Quartin (2014), \mathbf{C}_i was calculated analytically based on observations of higher moments of the SN residuals. However, in Macaulay et al. (2017), we found that the necessity of the analytical estimation of the data covariance matrix on measurements of high moments (up to the 8th) could lead to biases in the estimation of \mathbf{C}_i . Instead, we adopted a bootstrap re-sampling method, based only on the directly observed moments (i.e. up to the fourth). This bootstrap resampling method naturally allows for the covariance to be estimated between different types of observables, which is the approach we take here to include covariance between observations of the correlation function and the skewness of the SN.

2.2 Correlations

The correlation function of magnitude residuals due to weak lensing is given by

$$\langle \Delta \mu_i, \Delta \mu_j \rangle = \left(\frac{5}{\ln 10} \right)^2 \left(\frac{1}{2\pi} \right) \int_0^\infty \ell P_\kappa(\ell) J_0(\ell \Theta) d\ell, \quad (3)$$

where J_0 is the Bessel function of the zeroth kind (Bartelmann & Schneider 2001). $P_\kappa(\ell)$ is the angular power spectrum of the lensing convergence, κ , which is related to the matter power spectrum P_δ by

$$P_\kappa(\ell) = \frac{9H_0^4 \Omega_m^2}{4c^4} \int_0^{z_H} d\chi \frac{W^2(\chi)}{a^2(\chi)} P_\delta \left(\frac{\ell}{\chi}, \chi \right), \quad (4)$$

where W is the redshift distribution of the sources, and a is the scale factor, both as a function of comoving distance, χ . H_0 is the Hubble parameter, Ω_m is the total matter density, and c is the speed of light. We calculate $P_\kappa(\ell)$ with `CAMBsources` (Challinor & Lewis 2011), based on the redshift distribution of the SNe. To quantify the SNe redshift distribution, we use kernel density estimation (KDE) based on the redshifts of the SNe.

In this work, we focus on small scale ($\Theta < 30 \text{ arcmin}$) angular correlations. This is because the strongest correlation is expected at $\Theta < 10 \text{ arcmin}$ scales (as can be seen in Fig. 3).

2.3 Combined observations likelihood

In this paper, we simultaneously fit for the correlation and skewness caused by gravitational lensing, by minimizing the χ^2 given by

$$\chi^2 = \boldsymbol{\Delta}_\mu \mathbf{C}^{-1} \boldsymbol{\Delta}_\mu^T, \quad (5)$$

where (as with MeMo), $\boldsymbol{\Delta}_\mu$ is the difference between theory and observation vectors. We note that since our estimate of the data covariance matrix does not depend on σ_8 , minimizing this χ^2 is equivalent to likelihood maximization (for a fixed data covariance matrix). The vector $\boldsymbol{\mu}$ is constructed by concatenating the vectors for the two different types of observations:

$$\boldsymbol{\mu} = [\boldsymbol{\mu}_{ij}, \boldsymbol{\mu}_3], \quad (6)$$

where $\boldsymbol{\mu}_{ij}$ is the correlation vector (as a function of angular separation), and $\boldsymbol{\mu}_3$ is the third moment vector (as a function of redshift). We use four bins of angular separation and five redshift bins.

We choose the redshift binning to match the redshift bins in Abbott et al. (2019; within the redshift range used here). We have verified that the method is stable when changing the number of redshift or angular bins. This stability is aided by the bootstrap-resampling method used to estimate the covariance matrix: increasing the number of bins naturally increases the correlations in the off-diagonal elements of the covariance matrix.

We do not include the second and fourth moments, since the unique lensing skewness is captured by the third moment, and the even moments are sensitive to the model of the SN intrinsic dispersion. The implicit assumption of this choice is that the intrinsic dispersion of the magnitudes has zero skewness. We use `emcee` (Foreman-Mackey et al. 2013) to probe our likelihood.

2.4 Covariance matrix

In a similar manner to Macaulay et al. (2017), we use a bootstrap re-sampling method to estimate the data covariance matrix. To estimate

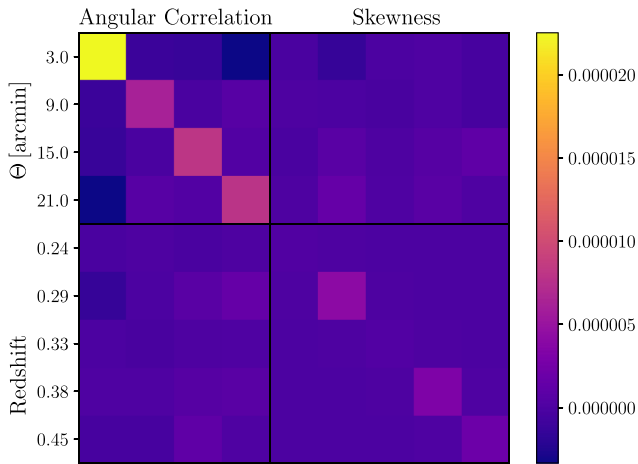


Figure 2. Illustrating the data covariance matrix. The upper left corner of the matrix is from the angular correlation function, and the lower right corner is from the skewness measurements. The bootstrap resampling method we use to estimate the covariance matrix allows us to estimate the cross-correlations between these two types of observable, shown in the off diagonal blocks.

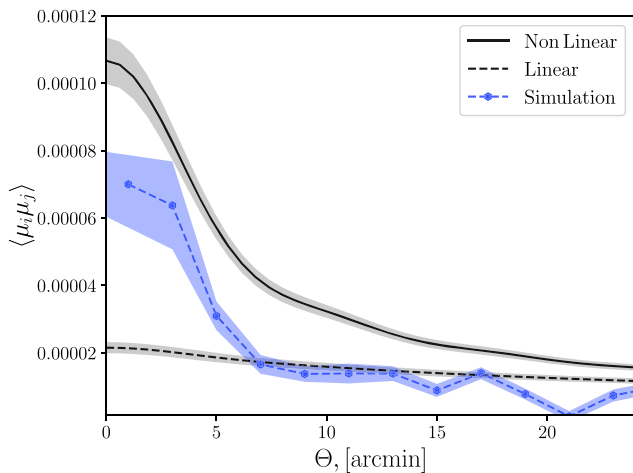


Figure 3. Measurements of the lensing correlation function measured from the MICE simulation to theoretical expectations from CAMBsources. The solid black line is the expected correlation function assuming a non-linear power spectrum, and the black-dashed line assumes a linear power spectrum. The grey-shaded regions illustrate the one standard deviation regions of these functions, due to small differences in the redshift distributions of each realization. The blue hexagonal points illustrate the average measured lensing correlation function from the MICE simulation.

C, we randomly sample (with replacement) from the genuine sample of SNe Ia. For each random sample, we calculate a combined data vector, consisting of the correlation and skewness vectors. We repeat this process of sampling to generate an ensemble of measurements, from which we can directly calculate an estimate of the covariance matrix. The advantage of this approach is that we can naturally estimate the covariance between the two different types of observable (the correlation and the skewness). The data covariance matrix is illustrated in Fig. 2.

2.5 Simulations

To verify our methodology against a fiducial cosmology, we generate realizations of DES–SN by drawing samples from the MICE simulation (Fosalba et al. 2015) with selection functions to match the genuine observations. We note that we use the simulations only as a test of the methodology; they do not directly contribute to the analysis of the genuine data (e.g. we do not use the simulations to estimate the data covariance matrix, etc.).

We start with a 3000 deg^2 light-cone from MICE, comprising over one million simulated galaxies. We then perform an angular selection cut, to match the 30 deg^2 area of the SN fields in DES. We match the footprints of the DES SNe fields, e.g. three patches for the C and X fields, and two for the E and S fields, so that the angular footprint matches the genuine DES fields. Over 10 000 simulated galaxies pass this angular selection cut.

We next sub-sample to match the number and redshift distribution of DES–SN. We approximate the redshift probability distribution function of DES–SN with a 1D KDE in redshift. To generate each simulated realization, we then draw 196 galaxies from the supersample of 10 000, with a probability ascribed to each galaxy given by the 1D KDE. Each realization thus matches the angular and redshift distribution of the genuine sample.

For each of these galaxies, we take the value of the lensing convergence, κ , as estimated by the MICE simulation, and calculate the magnitude residual Δ_μ due to κ , using

$$\Delta_\mu = 5 \log_{10}(1 - \kappa) \quad (7)$$

(Bartelmann & Schneider 2001). To include the effect of the intrinsic dispersion for a SN, we then add to the lensed-only residual Δ_μ a noise term, sampled from a Gaussian distribution (with standard deviation of 0.1 mag). This Δ_μ thus approximates a SN magnitude residual, including the intrinsic dispersion and lensing magnification.

In Fig. 3, we illustrate the measured correlation function from the MICE simulations. Since the signal from each realization is low, we measure the correlation function for 10 000 realizations, and show the average. We compare the simulated measurements to the expected theoretical linear and non-linear correlation function for the fiducial cosmology used in the MICE simulation.

The theoretical correlation function depends on the redshift distribution of the sources, which varies between realizations due to sampling noise. We re-calculate the theory for each redshift distribution, and illustrate the range in Fig. 3.

We can see in Fig. 3 that MICE most closely matches the linear theory for angular scales of $\Theta > 6$ arcmin. For smaller angular scales, MICE is closer to the non-linear theory. This may be due to the resolution of the MICE simulation.

MICE is based on a GADGET-2 simulation (Springel 2005) with a box width of $3072 h^{-1} \text{ Mpc}$, and a softening length of $50 h^{-1} \text{ kpc}$. To construct the simulated light-cones Fosalba et al. (2015) sample the simulation into 265 radially concentric ‘onion shells’ over the redshift range $0 < z < 1.4$, each corresponding to a time of approximately 35 megayears per shell. To calculate the lensing convergence maps, Fosalba et al. (2015) pixelate each shell using a Healpix angular tessellation with a Healpix resolution of $N_{\text{side}} = 4096$. This tessellation corresponds to an effective angular resolution of 0.85 arcmin. This resolution remains constant in redshift, since each shell is tessellated with the same $N_{\text{side}} = 4096$. This limit may be too coarse to fully resolve the rare, dense structures predicted by the theoretical non-linear correlation function.

Even though the resolution of the MICE simulation is 0.85 arcmin, we believe there are at least two effects that may introduce suppression of the correlation function out to angular scales larger than the resolution limit. First, feedback from smaller scales will not be able to affect structure formation at larger scales. In other words, the simulation will not resolve additional gravitational accretion from dense, sub-resolution structures. Secondly, even if structure at scales greater than 0.85 arcmin were perfectly resolved, we would still expect the correlation function to be underestimated for these scales, if the density of structure at sub-resolution scales remains underestimated, since the correlation function depends on the product of the densities across a range of angular scales.

We note that Fosalba et al. (2015) also find that for angular scales approaching 1 arcmin ($\ell \sim 10\,000$), the convergence power spectrum underestimates the non-linear theoretical expectation by ~ 30 per cent. This divergence can be seen in fig. 2 of Fosalba et al. (2015), particularly for ℓ close to 10 000.

We note that since the correlation function is an integral of the power spectrum across a range of scales, if the power spectrum is systematically underestimated across the range of integration, a given scale in the correlation function will be underestimated by a greater amount than the direct value of the power spectrum at the direct scale corresponding to the scale in the correlation function. We believe this is consistent with the results in Fig. 3 for the angular correlation function from the MICE simulation.

We believe there is a clear opportunity for future work to improve simulation of the small-scale lensing convergence power spectrum. However, we emphasize that since the current data places only large upper limits on the correlation function, this is not a limiting factor for this analysis.

When fitting for the correlation function, we assume a fiducial form for the function (given by the background cosmology and redshift distribution of the sources), and scale the amplitude according to the value of σ_8 . To fit for the genuine data, we use CAMBSources to calculate the matter power spectrum and lensing window function, with HALOFIT (Smith et al. 2003) to calculate the non-linear power spectrum.

However, we can see in Fig. 3 that this will overpredict the lensing signal in the simulated data. As such, when we fit for simulated catalogues, instead of using either the linear or non-linear correlation functions, we take the ensemble average correlation function in Fig. 3 as the fiducial.

Although we parametrize the amplitude of the density perturbations with σ_8 , we note that the physical scale of the density perturbations which affect SN lensing are at smaller physical scales (or higher k values, in the case of the power spectrum) than the 8 Mpc scale directly associated with σ_8 . Our assumption is that once we have set the amplitude of the density perturbations (via σ_8), we can extrapolate the scale of density fluctuations to smaller scales. Our use of σ_8 as a parameter is to set the relative scale of the density fluctuations, and not necessarily as a direct probe of structure at 8 Mpc scales.

We also test the skewness from the MICE simulation against the theoretical expectation from MeMo, shown in Fig. 4. We find that for $z > 0.5$ the MICE simulation underpredicts the effect of lensing moments compared to the MeMo fitting function.

We believe this is consistent with the underprediction of correlations at small angular scales seen in Fig. 3. Both the high z skewness and the small Θ correlation function rely on the simulation of small, rare, dense lines of sight, which demand high simulation resolution, and accurate modelling of the complicated baryonic physics that affects these small scales.

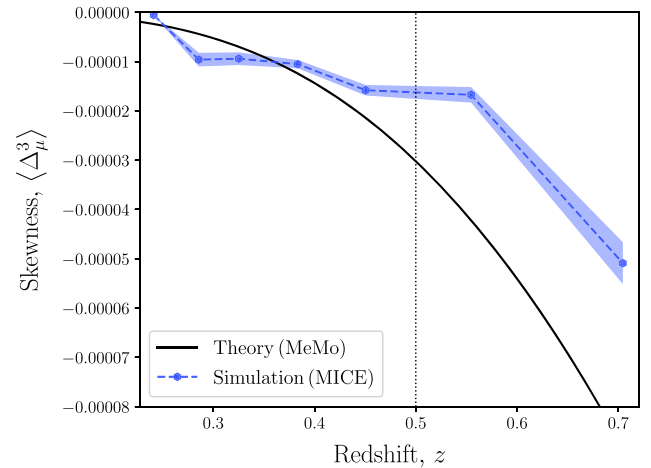


Figure 4. In this figure, we compare measurements of the lensing skewness from the MICE simulation to the corresponding theory from the MeMo fitting function. We note that MICE appears to underpredict the skewness, compared to the MeMo fitting function for $z > 0.5$.

Castro et al. (2018) found that introducing baryons has a significant effect on the lensing probability density function (although at scales that would not be resolved by the 0.85 arcmin resolution of MICE).

As we consider the lensing signal for lines of sight at increasingly high redshift, the chance of finding a rare, dense structure (causing high magnification) will increase. If these structures are not resolved in the simulation, we would expect the measured skewness to be less than expectations. As such, we do not fit for any moments for SNe with $z > 0.5$ for the real or simulated data sets. Although this redshift cut reduces our sensitivity to the most highly lensed SNe, the sparseness of the DES–SN sample at these redshifts also makes robust measurements of the skewness difficult.

3 DISCUSSION OF RESULTS AND CONCLUSIONS

The results of the fits to 100 simulated data sets are shown in Fig. 5. We plot the likelihood for each simulation, and also illustrate the average of the likelihoods, to verify that the results are consistent with the input of the simulation.

We note that the simulated realizations tend to cluster in two groups: a large fraction that recovers a lower value of σ_8 than the simulation input, and a small fraction that recovers a higher value. We believe that this is because of the non-Gaussian lensing probability distribution function, combined with the limited size of each realization. Due to the low likelihood of sampling from the high magnification tail, many of the realizations of 196 SNe will not have any samples drawn with high magnification, which will lead to low values of σ_8 . Conversely, a minority of the samples will have several magnified SNe, leading to an overestimated value of σ_8 . We believe this causes the distribution of simulated realizations in Fig. 5; with many realizations underestimating σ_8 , and a smaller sample overestimating σ_8 . However, we note that the ensemble average of the realizations is not biased.

We also show in Fig. 5 the equivalent fit to the genuine DES–SN data. We find $\sigma_8 = 1.2_{-0.8}^{+0.9}$, suggesting a possibility for WL at the $\sim 1.3\sigma$ level. We note that the uncertainty of our measurement is consistent with the uncertainties from the simulated data. In

Table 1. A summary of σ_8 measurements with SN–WL. We note that with the same method, DES–SN achieves smaller uncertainty than JLA, despite being a smaller sample. We also note in a comparison of methods (both with JLA), that the method in this work achieves similar uncertainty to that of Macaulay et al. (2017), without the imposition of a constant, Gaussian model for the SN intrinsic dispersion. Although the smallest uncertainties in this comparison are from Castro & Quartin (2014), we note that this work makes the least conservative assumptions here as to the measurements of the moments, and the estimation of the data-covariance matrix (as discussed further in Macaulay et al. 2017).

Reference	Sample	Method	σ_8 Value
Castro & Quartin (2014)	JLA	Variance+Skewness+Kurtosis	$0.8^{+0.3}_{-0.7}$
Macaulay et al. (2017)	JLA	Variance+Skewness+Kurtosis	$1.6^{+0.5}_{-1.0}$
This Work	JLA	Skewness+Correlation	$0.8^{+1.1}_{-0.7}$
This Work	DES–SN	Skewness+Correlation	$1.2^{+0.9}_{-0.8}$

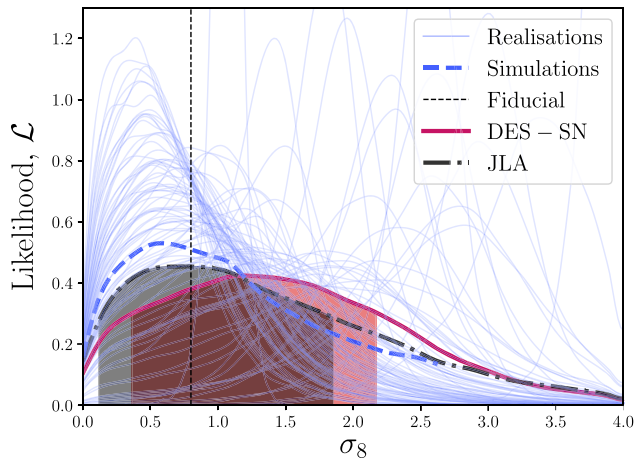


Figure 5. Constraints on σ_8 from the genuine DES–SN sample, and also simulated realizations of the sample. Individual fits to simulated realizations are shown in thin blue lines, and the average of these fits is shown with a thick, blue-dashed line. The input value of σ_8 used in the simulation is shown with the thin, black vertical dashed line. The thick red line illustrates the constraints from the genuine sample, with the one-standard deviation uncertainty range shown with the shaded region.

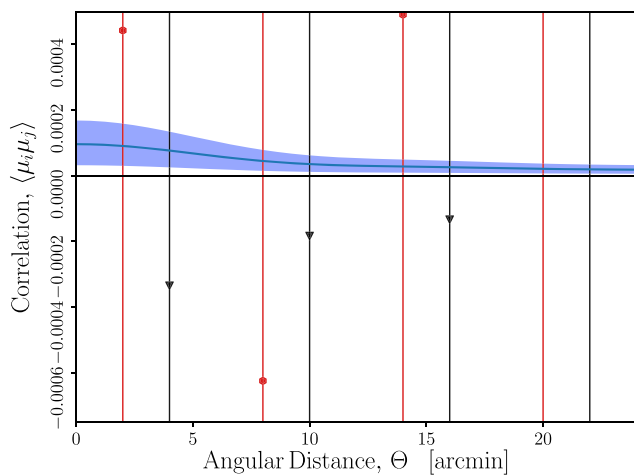


Figure 6. The observed angular correlation function of the JLA and DES–SN samples. The fiducial angular correlation function is illustrated with the blue line, and the allowed range of σ_8 from DES–SN is shown with the shaded region. We note that the measured points are highly correlated, and in some cases we can place only upper limits on the angular correlation function.

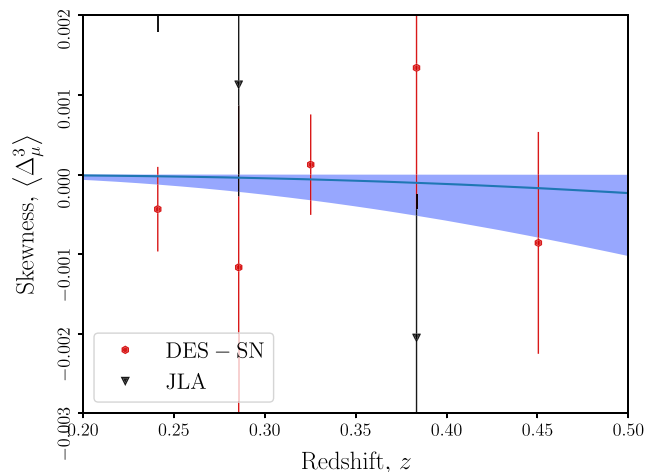


Figure 7. The measured skewness of the JLA and DES–SN samples. The blue-shaded region illustrates the range of lensing skewness given the range of the best-fitting σ_8 from the DES–SN sample ($\sigma_8 = 1.2^{+0.9}_{-0.8}$).

Figs 6 and 7, we plot the observed angular correlation function and skewness for DES–SN.

Albeit within large (~ 100 per cent) uncertainties, we note that our value is consistent with the value of $\sigma_8 = 0.8120 \pm 0.0073$ derived by Planck Collaboration VI (2018a) from measurements of the CMB, assuming a Λ CDM model. The values are summarised in Table 1.

Perhaps of more significance than the best-fitting value of σ_8 , we emphasize the lower limit of 0.4. We note that this lower limit is not sensitive to the value of the intrinsic dispersion of the SNe Ia, as with, e.g. Castro & Quartin (2014) and Macaulay et al. (2017). We assume only that the intrinsic dispersion is uncorrelated (i.e. genuinely intrinsic to each SN), and does not introduce additional skewness. Beyond these assumptions, the model requires no further assumption as to the intrinsic dispersion of the SNe (such as redshift independence).

Although far from a detection of WL in SNe, this lower limit on σ_8 suggests some possibility for WL, consistent with the statistical limitations of the size of the sample (e.g. Scovacricchi et al. 2017). We note that the limits on WL is consistent with the lensing results found by Smith et al. (2014), who found limits on the lensing signal with a significance of 1.7σ . The value of σ_8 and significance of the lensing signal is also consistent with the values from Macaulay et al. (2017).

We repeat our measurement with the JLA sample. As with DES–SN, we restrict the redshift range to $z > 0.17$, to minimize sensitivity

to PV. We also restrict the redshift range to $z < 0.5$ (again, as with DES–SN), since we believe that the systematic uncertainties in theoretical modelling and simulation of extreme-small-scale weak lensing at high redshift is currently insufficient, even given the large statistical uncertainties of WL in current SNe surveys. After these redshift cuts, we have 488 SNe from the JLA sample, and find $\sigma_8 = 0.8_{-0.7}^{+1.1}$.

We note that the range of uncertainty σ_8 from JLA of 1.8 is larger than the range from DES–SN, of 1.7, despite the larger number of 488 SNe in the JLA sub-sample than the 196 from DES. We believe this is due to the homogeneity of the DES–SN sample, and improvements in photometric calibration.

We note that our values with both DES–SN and JLA are consistent with the value from Castro & Quartin (2014), studying JLA, who found $\sigma_8 = 0.84_{-0.65}^{+0.28}$. Comparing directly to our value with JLA of $\sigma_8 = 0.8_{-0.7}^{+1.1}$, we note that although our uncertainty is larger, there are several differences between the two analyses.

In this work, we do not include SNe at $z > 0.5$, and do not include the second and fourth moments. Also, while the bootstrap resampling method we use here to estimate the data-covariance matrix allows us to estimate the covariance between the third moment and the correlation function, this method leads to larger uncertainties than the analytical covariance matrix used by Castro & Quartin (2014).

Although the statistical uncertainty on the value of σ_8 is far from competitive with lensing measurements from galaxy shear techniques, we note the added value nature of the measurement; placing limits on WL from observations taken to probe the distance–redshift relation.

We reiterate the conclusions from Scovacricchi et al. (2017) of the potential to place competitive constraints on WL with the next generations of SNe surveys, such as LSST (LSST Science Collaboration 2009; LSST Dark Energy Science Collaboration 2012; Ivezić et al. 2019), *Euclid* (Laureijs et al. 2011; Astier et al. 2014; Amendola et al. 2018), and *WFIRST* (Hounsell et al. 2018). We also emphasize the need for improved modelling of simulations and theory of the high redshift, small angular-scale lensing effects that will be required to fully realize the potential for SN–WL.

ACKNOWLEDGEMENTS

We thank the referee for a careful review, and constructive comments and suggestions, which have been very helpful in improving this work.

EM, DB, RCN acknowledge funding from STFC grant ST/N000668/1.

This paper has used observations taken using the Anglo-Australian Telescope under programs ATAC A/2013B/12 and NOAO 2013B-0317; the Gemini Observatory under programs NOAO 2013A-0373/GS-2013B-Q-45, NOAO 2015B-0197/GS-2015B-Q-7, and GS-2015B-Q-8; the Gran Telescopio Canarias under programs GTC77-13B, GTC70-14B, and GTC101-15B; the Keck Observatory under programs U063-2013B, U021-2014B, U048-2015B, U038-2016A; the Magellan Observatory under programs CN2015B-89; the MMT under 2014c-SAO-4, 2015a-SAO-12, 2015c-SAO-21; the South African Large Telescope under programs 2013-1-RSA_OTH-023, 2013-2-RSA_OTH-018, 2014-1-RSA_OTH-016, 2014-2-SCI-070, 2015-1-SCI-063, and 2015-2-SCI-061; and the Very Large Telescope under programs ESO 093.A-0749(A), 094.A-0310(B), 095.A-0316(A), 096.A-0536(A), 095.D-0797(A).

Funding for the DES Projects has been provided by the U.S. Department of Energy, the U.S. National Science Foundation, the Ministry of Science and Education of Spain, the Science and Technology Facilities Council of the United Kingdom, the Higher Education Funding Council for England, the National Center for Supercomputing Applications at the University of Illinois at Urbana-Champaign, the Kavli Institute of Cosmological Physics at the University of Chicago, the Center for Cosmology and AstroParticle Physics at the Ohio State University, the Mitchell Institute for Fundamental Physics and Astronomy at Texas A&M University, Financiadora de Estudos e Projetos, Fundação Carlos Chagas Filho de Amparo à Pesquisa do Estado do Rio de Janeiro, Conselho Nacional de Desenvolvimento Científico e Tecnológico and the Ministério da Ciência, Tecnologia e Inovação, the Deutsche Forschungsgemeinschaft, and the Collaborating Institutions in the DES.

The Collaborating Institutions are Argonne National Laboratory, the University of California at Santa Cruz, the University of Cambridge, Centro de Investigaciones Energéticas, Medioambientales y Tecnológicas, the University of Chicago, University College London, the DES-Brazil Consortium, the University of Edinburgh, the Eidgenössische Technische Hochschule Zürich, Fermi National Accelerator Laboratory, the University of Illinois at Urbana-Champaign, the Institut de Ciències de l’Espai (IEEC/CSIC), the Institut de Física d’Altes Energies, Lawrence Berkeley National Laboratory, the Ludwig-Maximilians-Universität München and the associated Excellence Cluster Universe, the University of Michigan, the National Optical Astronomy Observatory, the University of Nottingham, The Ohio State University, the University of Pennsylvania, the University of Portsmouth, SLAC National Accelerator Laboratory, Stanford University, the University of Sussex, Texas A&M University, and the OzDES Membership Consortium.

Based in part on observations at Cerro Tololo Inter-American Observatory, National Optical Astronomy Observatory, which is operated by the Association of Universities for Research in Astronomy under a cooperative agreement with the National Science Foundation.

The DES data management system is supported by the National Science Foundation under grants AST-1138766 and AST-1536171. The DES participants from Spanish institutions are partially supported by MINECO under grants AYA2015-71825, ESP2015-66861, FPA2015-68048, SEV-2016-0588, SEV-2016-0597, and MDM-2015-0509, some of which include ERDF funds from the European Union. IFAE is partially funded by the CERCA program of the Generalitat de Catalunya. Research leading to these results has received funding from the European Research Council under the European Union’s Seventh Framework Program (FP7/2007-2013) including ERC grant agreements 240672, 291329, and 306478. We acknowledge support from the Australian Research Council Centre of Excellence for All-sky Astrophysics (CAASTRO), through project number CE110001020, and the Brazilian Instituto Nacional de Ciência e Tecnologia (INCT) e-Universe (CNPq grant 465376/2014-2).

This manuscript has been authored by Fermi Research Alliance, LLC under Contract No. DE-AC02-07CH11359 with the U.S. Department of Energy, Office of Science, Office of High Energy Physics. The United States Government retains and the publisher, by accepting the article for publication, acknowledges that the United States Government retains a non-exclusive, paid-up, irrevocable, world-wide license to publish or reproduce the published form of this manuscript, or allow others to do so, for United States Government purposes.

DATA AVAILABILITY

The SN data underlying this article were accessed from <https://des.ncsa.illinois.edu/releases/sn>. The simulated data were accessed from <http://maia.ice.cat/mice/>.

REFERENCES

- Abbott T. et al., 2016, *Phys. Rev. D*, 94, 022001
- Abbott T. M. C. et al., 2018, *Phys. Rev. D*, 98, 043526
- Abbott T. M. C. et al., 2019, *ApJ*, 872, L30
- Amendola L. et al., 2018, *Living Rev. Relativ.*, 21, 2
- Astier P. et al., 2014, *A&A*, 572, A80
- Bartelmann M., Schneider P., 2001, *Phys. Rep.*, 340, 291
- Bauer A. H., Seitz S., Jerke J., Scalzo R., Rabinowitz D., Ellman N., Baltay C., 2011, *ApJ*, 732, 64
- Baxter E. J. et al., 2019, *Phys. Rev. D*, 99, 023508
- Becker M. R. et al., 2016, *Phys. Rev. D*, 94, 022002
- Bertschinger E., Zukin P., 2008, *Phys. Rev. D*, 78, 024015
- Betoule M. et al., 2014, *A&A*, 568, A22
- Brout D. et al., 2019a, *ApJ*, 874, 106
- Brout D. et al., 2019b, *ApJ*, 874, 150
- Castro T., Quartin M., 2014, *MNRAS*, 443, L6
- Castro T., Quartin M., Benitez-Herrera S., 2016, *Phys. Dark Universe*, 13, 66
- Castro T., Quartin M., Giocoli C., Borgani S., Dolag K., 2018, *MNRAS*, 478, 1305
- Challinor A., Lewis A., 2011, *Phys. Rev. D*, 84, 043516
- D'Andrea C. B. et al., 2018, preprint ([arXiv:1811.09565](https://arxiv.org/abs/1811.09565))
- Davis T. M. et al., 2011, *ApJ*, 741, 67
- Dawson K. S. et al., 2013, *AJ*, 145, 10
- Dodelson S., Vallinotto A., 2006, *Phys. Rev. D*, 74, 063515
- Foreman-Mackey D., Hogg D. W., Lang D., Goodman J., 2013, *PASP*, 125, 306
- Fosalba P., Gaztañaga E., Castander F. J., Crocce M., 2015, *MNRAS*, 447, 1319
- Garcia K., Quartin M., Siffert B. B., 2019, *Phys. Dark Universe*, 29, 100519
- Gordon C., Land K., Slosar A., 2007, *Phys. Rev. Lett.*, 99, 081301
- Heymans C. et al., 2012, *MNRAS*, 427, 146
- Hilbert S., White S. D. M., Hartlap J., Schneider P., 2008, *MNRAS*, 386, 1845
- Hildebrandt H. et al., 2017, *MNRAS*, 465, 1454
- Hounsell R. et al., 2018, *ApJ*, 867, 23
- Hu W., Jain B., 2004, *Phys. Rev. D*, 70, 043009
- Ivezić, Ž. et al., 2019, *ApJ*, 873, 111
- Joudaki S. et al., 2017, *MNRAS*, 471, 1259
- Kainulainen K., Marra V., 2009, *Phys. Rev. D*, 80, 123020
- Kainulainen K., Marra V., 2011, *Phys. Rev. D*, 83, 023009
- Kessler R. et al., 2019, *MNRAS*, 485, 1171
- Knox L., Song Y.-S., Tyson J. A., 2006, *Phys. Rev. D*, 74, 023512
- Kunz M., Sapone D., 2007, *Phys. Rev. Lett.*, 98, 121301
- Lasker J. et al., 2019, *MNRAS*, 485, 5329
- Laureijs R. et al., 2011, preprint ([arXiv:1110.3193](https://arxiv.org/abs/1110.3193))
- Liao K., Fan X.-L., Ding X., Biesiada M., Zhu Z.-H., 2017, *Nat. Commun.*, 8, 1148
- LSST Dark Energy Science Collaboration, 2012, preprint ([arXiv:1211.0310](https://arxiv.org/abs/1211.0310))
- LSST Science Collaboration, 2009, preprint ([arXiv:0912.0201](https://arxiv.org/abs/0912.0201))
- Macaulay E., Davis T. M., Scovaccicchi D., Bacon D., Collett T., Nichol R. C., 2017, *MNRAS*, 467, 259
- Marra V., Quartin M., Amendola L., 2013, *Phys. Rev. D*, 88, 063004
- Neill J. D., Hudson M. J., Conley A., 2007, *ApJ*, 661, L123
- Omori Y. et al., 2018, *Phys. Rev. D*, 100, 043517
- Planck Collaboration VI, 2018a, preprint ([arXiv:1807.06209](https://arxiv.org/abs/1807.06209))
- Planck Collaboration VIII, 2018b, preprint ([arXiv:1807.06210](https://arxiv.org/abs/1807.06210))
- Quartin M., Marra V., Amendola L., 2014, *Phys. Rev. D*, 89, 023009
- Schimd C., Uzan J.-P., Riazuelo A., 2005, *Phys. Rev. D*, 71, 083512
- Schimd C. et al., 2007, *A&A*, 463, 405
- Schmidt F., 2008, *Phys. Rev. D*, 78, 043002
- Schrabback T. et al., 2010, *A&A*, 516, A63
- Scovaccicchi D., Nichol R. C., Macaulay E., Bacon D., 2017, *MNRAS*, 465, 2862
- Scranton R. et al., 2005, *ApJ*, 633, 589
- Shang C., Haiman Z., 2011, *MNRAS*, 411, 9
- Simpson F. et al., 2013, *MNRAS*, 429, 2249
- Smith R. E. et al., 2003, *MNRAS*, 341, 1311
- Smith M. et al., 2014, *ApJ*, 780, 24
- Springel V., 2005, *MNRAS*, 364, 1105
- Takahashi R., Oguri M., Sato M., Hamana T., 2011, *ApJ*, 742, 15
- The Dark Energy Survey Collaboration, 2005, preprint ([astro-ph/0510346](https://arxiv.org/abs/astro-ph/0510346))
- Troxel M. A. et al., 2018, *Phys. Rev. D*, 98, 043528
- Tsujikawa S., Tatekawa T., 2008, *Phys. Lett. B*, 665, 325
- Valageas P., 2000, *A&A*, 356, 771
- Wambsgans J., Cen R., Xu G., Ostriker J. P., 1997, *ApJ*, 475, L81
- Wang Y., 2005, *J. Cosmol. Astropart. Phys.*, 2005, 005
- Wang Y., Mukherjee P., 2004, *ApJ*, 606, 654
- Wittman D. M., Tyson J. A., Kirkman D., Dell'Antonio I., Bernstein G., 2000, *Nature*, 405, 143
- Zhang P., Liguori M., Bean R., Dodelson S., 2007, *Phys. Rev. Lett.*, 99, 141302
- Zuntz J. et al., 2018, *MNRAS*, 481, 1149

¹Department of Physics and Astronomy, University of North Georgia, Dahlonega, GA, USA

²Institute of Cosmology and Gravitation, University of Portsmouth, Portsmouth PO1 3FX, UK

³School of Mathematics and Physics, University of Queensland, Brisbane, QLD 4072, Australia

⁴Center for Cosmology and Astro-Particle Physics, The Ohio State University, Columbus, OH 43210, USA

⁵Department of Physics, The Ohio State University, Columbus, OH 43210, USA

⁶NASA Einstein Fellow

⁷Department of Physics and Astronomy, University of Pennsylvania, Philadelphia, PA 19104, USA

⁸INAF, Astrophysical Observatory of Turin, I-10025 Pino Torinese, Italy

⁹Centre for Astrophysics & Supercomputing, Swinburne University of Technology, VIC 3122, Australia

¹⁰Sydney Institute for Astronomy, School of Physics, A28, The University of Sydney, NSW 2006, Australia

¹¹The Research School of Astronomy and Astrophysics, Australian National University, ACT 2601, Australia

¹²Université Clermont Auvergne, CNRS/IN2P3, LPC, F-63000 Clermont-Ferrand, France

¹³Department of Physics, Duke University Durham, NC 27708, USA

¹⁴School of Physics and Astronomy, University of Southampton, Southampton SO17 1BJ, UK

¹⁵Cerro Tololo Inter-American Observatory, National Optical Astronomy Observatory, Casilla 603, La Serena, Chile

¹⁶Departamento de Física Matemática, Instituto de Física, Universidade de São Paulo, CP 66318, São Paulo, SP 05314-970, Brazil

¹⁷Laboratório Interinstitucional de e-Astronomia - LIneA, Rua Gal. José Cristino 77, Rio de Janeiro, RJ - 20921-400, Brazil

¹⁸Fermi National Accelerator Laboratory, PO Box 500, Batavia, IL 60510, USA

¹⁹Instituto de Física Teórica UAM/CSIC, Universidad Autonoma de Madrid, E-28049 Madrid, Spain

²⁰CNRS, UMR 7095, Institut d'Astrophysique de Paris, F-75014 Paris, France

²¹Sorbonne Universités, UPMC Univ Paris 06, UMR 7095, Institut d'Astrophysique de Paris, F-75014 Paris, France

²²Department of Physics and Astronomy, Pevensey Building, University of Sussex, Brighton BN1 9QH, UK

²³Department of Physics & Astronomy, University College London, Gower Street, London WC1E 6BT, UK

²⁴Kavli Institute for Particle Astrophysics & Cosmology, PO Box 2450, Stanford University, Stanford, CA 94305, USA

²⁵SLAC National Accelerator Laboratory, Menlo Park, CA 94025, USA

²⁶Centro de Investigaciones Energéticas, Medioambientales y Tecnológicas (CIEMAT), Madrid, Spain

²⁷Department of Astronomy, University of Illinois at Urbana-Champaign, 1002 W. Green Street, Urbana, IL 61801, USA

²⁸National Center for Supercomputing Applications, 1205 West Clark St., Urbana, IL 61801, USA

²⁹Institut de Física d'Altes Energies (IFAE), The Barcelona Institute of Science and Technology, Campus UAB, E-08193 Bellaterra (Barcelona) Spain

³⁰Institut d'Estudis Espacials de Catalunya (IEEC), E-08034 Barcelona, Spain

³¹Institute of Space Sciences (ICE, CSIC), Campus UAB, Carrer de Can Magrans, s/n, E-08193 Barcelona, Spain

³²INAF-Osservatorio Astronomico di Trieste, via G. B. Tiepolo 11, I-34143 Trieste, Italy

³³Institute for Fundamental Physics of the Universe, Via Beirut 2, I-34014 Trieste, Italy

³⁴Observatório Nacional, Rua Gal. José Cristino 77, Rio de Janeiro, RJ - 20921-400, Brazil

³⁵Department of Physics, IIT Hyderabad, Kandi, Telangana 502285, India

³⁶Santa Cruz Institute for Particle Physics, Santa Cruz, CA 95064, USA

³⁷Department of Astronomy, University of Michigan, Ann Arbor, MI 48109, USA

³⁸Department of Physics, University of Michigan, Ann Arbor, MI 48109, USA

³⁹Department of Physics, Stanford University, 382 Via Pueblo Mall, Stanford, CA 94305, USA

⁴⁰Center for Astrophysics | Harvard & Smithsonian, 60 Garden Street, Cambridge, MA 02138, USA

⁴¹Australian Astronomical Optics, Macquarie University, North Ryde, NSW 2113, Australia

⁴²Lowell Observatory, 1400 Mars Hill Rd, Flagstaff, AZ 86001, USA

⁴³George P. and Cynthia Woods Mitchell Institute for Fundamental Physics and Astronomy, and Department of Physics and Astronomy, Texas A&M University, College Station, TX 77843, USA

⁴⁴Department of Astrophysical Sciences, Princeton University, Peyton Hall, Princeton, NJ 08544, USA

⁴⁵Institució Catalana de Recerca i Estudis Avançats, E-08010 Barcelona, Spain

⁴⁶Kavli Institute for Cosmological Physics, University of Chicago, Chicago, IL 60637, USA

⁴⁷Department of Physics, Brandeis University, 415 South Street, Waltham, MA 02453, USA

⁴⁸Computer Science and Mathematics Division, Oak Ridge National Laboratory, Oak Ridge, TN 37831, USA

⁴⁹Max Planck Institute for Extraterrestrial Physics, Giessenbachstrasse, D-85748 Garching, Germany

⁵⁰Fakultät für Physik, Universitäts-Sternwarte, Ludwig-Maximilians-Universität München, Scheinerstr 1, D-81679 München, Germany

This paper has been typeset from a $\text{\TeX}/\text{\LaTeX}$ file prepared by the author.